Electronic Supplementary Material (ESI) for RSC Advances.

Field Effect Dominated Bipolar Resistive Switching through Interface Control in $Pt/TiO_2/TiN$ Structure

Dong-Hyeok Lim[1], Ga-Yeon Kim[1], Jin-Ho Song[1], Kwang-Sik Jeong[1], Dong Chan Kim[2], Seok-Woo Nam[2], Mann-Ho Cho[1], Tae-Geol Lee[3]*

[1]Institute of Physics and Applied Physics, Yonsei University, Seoul 120-749, Korea

[2]Process Development Team, Semiconductor R&D Division, Suwon 445-701, Korea

[3]Korea Research Institute of Standards and Science, Daejeon 305-340, Korea

KEYWORDS: RRAM, Titanium dioxide, Catalytic effect, Oxygen vacancy, Ionic movement

Supporting Information

1. XPS depth profile

To identify the initial differences between the $Pt/TiO_2/TiN$ and the $Pt/TiO_2/TiO_{2\rightarrow 2-x}/TiN$ (or simply $Pt/TiO_2/TiO_{2-x}/TiN$) structures, we performed depth profiling using X-ray photoelectron spectroscopy (XPS). The oxygen-1s spectrum was obtained through a repeated sputtering and measurement process on a Pt-free region. Figures S1(a) and (b) depict the different oxygen configurations in the depth direction in TiO_2/TiN and $TiO_2/TiO_{2\rightarrow 2-x}/TiN$. According to surface etching time, the measured region was divided into Sections I – V. After the topmost oxygen adsorption layer, Region I, was sputtered, the O-1s spectra showed almost the same peak

positions and total counts in Region II (Figs. S1(c) and (g) indicating each stoichiometric TiO_2 layer. In Region III, the intensity of the spectrum decreased due to oxygen deficiency (Fig. S1(d)) in $TiO_2/TiO_{2\rightarrow 2-x}/TiN$. As the etching continued, a peak with a high binding energy was observed, which we assigned to non-lattice oxygen implying the existence of oxygen vacancy (Fig. S1(e)).[1] Total count of detected photoelectrons was obtained by integrating the area of the spectrum in Fig. S1(f). The increase in the non-lattice oxygen peak, even with similar total electron counts in Region IV, indicated a large amount of non-lattice oxygen (or oxygen vacancies).

2. TEM and HAADF images for the fabricated samples

Transmission electron microscope (TEM) images for TiO_2/TiN case and $TiO_{2\rightarrow 2-x}/TiN$ (or simply TiO_{2-x}/TiN) are shown in Figs. S2(a) and (b), respectively. The stoichiometric TiO_2 shows brighter image and thus the TiO_2/TiN interface is clearly revealed. The boundary between $TiO_2/TiO_{2\rightarrow 2-x}$ inside the oxide could not be distinguished; however the brightest region at the Pt/TiO_2 interface indicates the additional oxidation layer detected by XPS. This can contribute the Schottky barrier formation. Figures S2(c) and (d) are low magnified images; (e) and (f) are the corresponding high angle annular dark field (HAADF) images. The smooth interface at the $TiO_{2\rightarrow 2-x}/TiN$ is observed as expected although the difference in oxygen content was not revealed by energy dispersive spectroscopy (EDS).

3. Simulation details

Figure S3(a) depicts the reaction-diffusion-drift process and the geometry of the model used in simulations. The reaction region was fixed at a point beneath the center of the top electrode to

avoid electrode edge effects[2] at this stage. Outputs of the simulation were the vacancy concentration and equipotential lines. Figure S3(b) describes the recursive sequence of the simulation. Conductivity at all (x, y) points was calculated using the conductivity function of vacancy concentration, $\sigma(n_v(x, y))$, according to the vacancy concentration, as shown in Fig. S3(c). To emphasize the effect of vacancy-dependent conductivity, various conductivity conditions were examined. All the parameters are determined as similar order of values obtained from other reported papers[3-6]. Because the vacancy concentration ranged from low (insulating state) to high (metallic states), vacancies were considered to be dependent on the threshold concentration and the maximum conductivity; we defined the threshold concentration as the concentration at which the oxygen vacant states became metallic. Maximum conductivity (gap between the maximum and the minimum due to the fixed minimum) revealed that the slope of rate of conductivity increased with an increase in vacancies. Conductivity functions, $F_0 - F_4$, were categorized according to n_v–σ relations. For example, the F_0 relation describes the situation where no field effect was induced by the presence of oxygen vacancies. In this case, the electric potential formed by the applied voltage was not affected by the vacancy distribution.

Based on the calculated conductivity, we calculated the electric potential $\varphi(x, y)$ with a boundary condition. Furthermore, drift velocity was calculated by taking the gradient of the electric potential $\nabla\varphi(x, y)$ at a certain time t.[7] Then, vacancies were relocated according to the calculated drift velocity and thus $n_v(x, y)$ were renewed during time interval Δt. Reaction and diffusion processes were introduced at this time and are reflected in $n_v(x, y)$. These procedures were repeated at time $t + \Delta t$ until specific conditions were satisfied. Figure S3(d) shows the different vacancy distributions at different times during the simulation. To determine how each term of the equation was affect by the presence or absence of vacancy concentration-dependent

conductivity, we compared several conditions: (i) reaction + n_v-independent drift (F_0), (ii) reaction + diffusion + n_v-independent drift (F_0), (iii) reaction + n_v-dependent drift (F_1), and (iv) reaction + diffusion + n_v-dependent drift (F_1). The brighter region and horizontal lines indicate a high vacancy concentration and equipotential lines, respectively. Each additional side view of the concentration is shown on the left. A comparison of (i) with (iii), and (ii) and (iv), revealed that the vacancy-concentration dependent drift process crucially affected vacancy movements. Furthermore, different n_v-dependent conductivity and mobility effects were examined: (v) high threshold concentration (F_2), (vi) small maximum conductivity (F_3), and (vii) high mobility. By comparing (iv) and (v), we observed that a high threshold concentration induced less dispersive vacancy movement at the bottom of the vacancies and a high concentration in the middle of the vacancies. Furthermore, by comparing (iv) and (vi), we observed that low maximum conductivity induced less dispersive vacancy movement at the bottom of the vacancies and a relatively low concentration in the middle of the vacancies. The high vacancy mobility case (vii) showed relatively fast movement compared with (iv). Together, these simulation results indicated that vacancy concentration-dependent conductivity can affect vacancy movement. Furthermore, it should be noted that material properties, such as vacancy-dependent conductivity and -mobility can be used to design a device with optimized vacancy movement.

4. Confirmation of the gradual change in the non-stoichiometry of the TiO_{2-x} layer.

Although it was hard to clearly confirm the change in non-stoichiometry of the TiO_{2-x} layer, TEM-EDS quantitative analysis and XPS depth-profiling showed the gradual change in TiO_{2-x} layer. The TEM-EDS results revealed gradually decreasing oxygen counts from the Pt electrode in the Pt/TiO_2/TiO_{2-x}/TiN, as shown in Figure. S4. It can be seen that *x* gradually increases in the

TiO_{2-x} layer because of a gradual decrease of oxygen. XPS depth-profiling analysis with Ne ion etching was also employed. Although the XPS depth profiling, as well as the FIB, has a sputtering process that results in some degree of error for the evaluation of stoichiometry, the gradual change in the decrease of lattice oxygen and the increase of non-lattice oxygen in TiO_{2-x} layer were observed. The XPS depth profiling result of the stoichiometric TiO_2 is shown in Figure S5. (The numbering means the sequence of measurements. Except the first measurement '1', the sputtering was carried out before the measurement with an etching rate of approximately 2 nm per sputtering.) Although the vertical spatial resolution is not good because of the small escape depth of the photoelectrons (about 7 nm vertically from the surface), comparison between the two spectra reveals the gradual oxygen deficiency in the TiO_{2-x} layer.

AUTHOR INFORMATION

Corresponding Author: mh.cho@yonsei.ac.kr

ACKNOWLEDGMENTS

This research was supported by the National Research Project for "Next Generation MLC PRAM Development" through the Ministry of Knowledge Economy (MKE) of Korea and by YSSRC program through Samsung Semiconductor Co.

REFERENCES

1. Sang-Joon, P.; Jeong-Pyo, L.; Jong Shik, J.; Hyun, R.; Hyunung, Y.; Byung Youn, Y.; Chang Soo, K.; Kyung Joong, K.; Yong Jai, C.; Sunggi, B.; Woo, L., In-Situ Control of Oxygen

Vacancies in TiO_2 by Atomic Layer Deposition for Resistive Switching Devices. *Nanotechnology* **2013,** *24* (29), 295202.

2. Yao, J.; Sun, Z.; Zhong, L.; Natelson, D.; Tour, J. M., Resistive Switches and Memories from Silicon Oxide. *Nano Letters* **2010,** *10* (10), 4105-4110.

3. Kim, S.; Choi, S.; Lu, W., Comprehensive Physical Model of Dynamic Resistive Switching in an Oxide Memristor. *ACS Nano* **2014,** *8* (3), 2369-2376.

4. Yu, S. M.; Wong, H. S. P., A Phenomenological Model for the Reset Mechanism of Metal Oxide RRAM. *Ieee Electron Device Letters* **2010,** *31* (12), 1455-1457.

5. Kim, S.; Kim, S.-J.; Kim, K. M.; Lee, S. R.; Chang, M.; Cho, E.; Kim, Y.-B.; Kim, C. J.; In Chung, U.; Yoo, I.-K., Physical Electro-Thermal Model of Resistive Switching in Bi-Layered Resistance-Change Memory. *Sci. Rep.* **2013,** *3*.

6. Larentis, S.; Nardi, F.; Balatti, S.; Gilmer, D. C.; Ielmini, D., Resistive Switching by Voltage-Driven Ion Migration in Bipolar RRAM-Part II: Modeling. *IEEE Trans. Electron Devices* **2012,** *59* (9), 2468-2475.

7. Strukov, D. B.; Williams, R. S., Exponential Ionic Drift: Fast Switching and Low Volatility of Thin-film Memristors. *Applied Physics a-Materials Science & Processing* **2009,** *94* (3), 515-519.

Figures

Figure S1

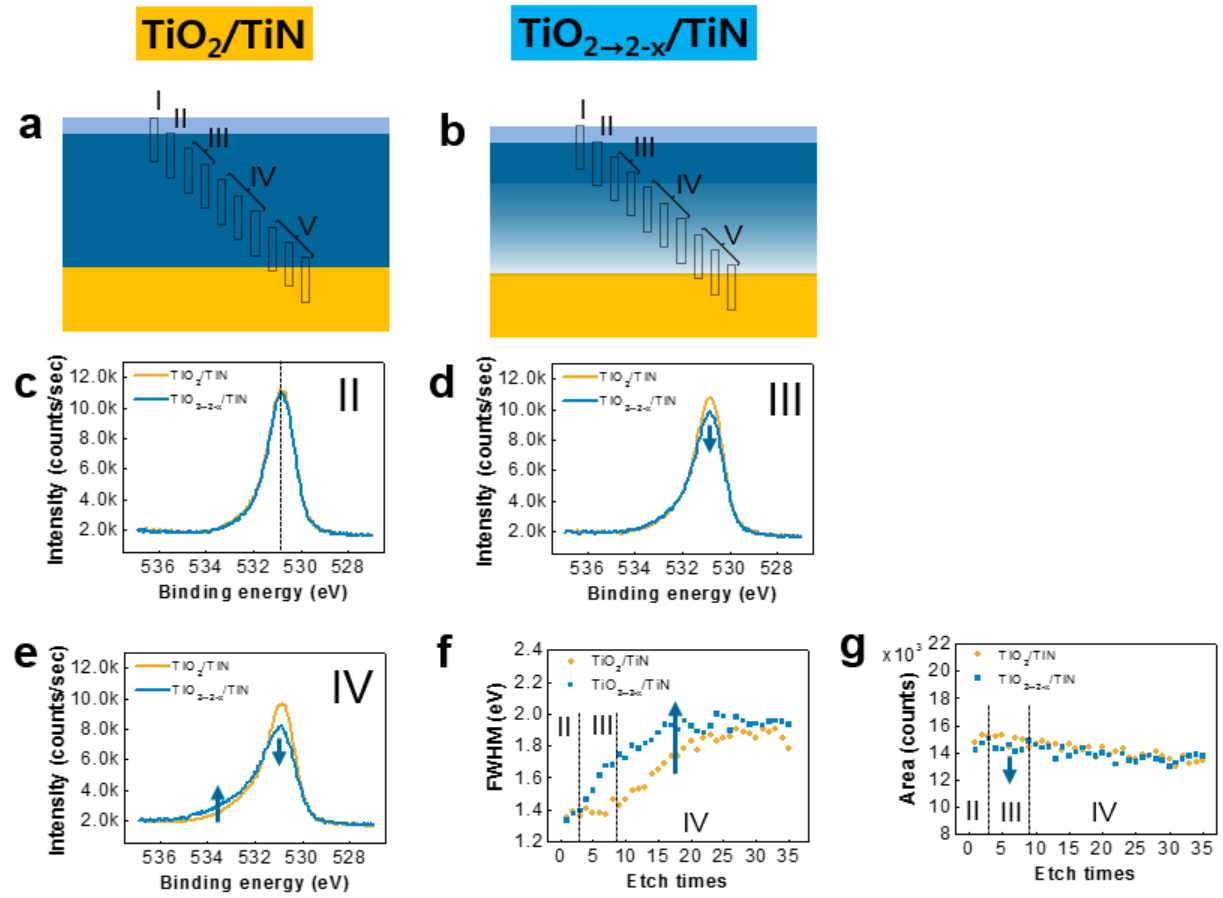
TiO2/TiN
TiO2→2-x/TiN
a
b
I
II
III
IV
V
c
d
e
f
g
Intensity (counts/sec)
Binding energy (eV)
FWHM (eV)
Etch times
Area (counts)
x10^3
TiO2/TiN
TiO2-2x/TiN

Figure S2.

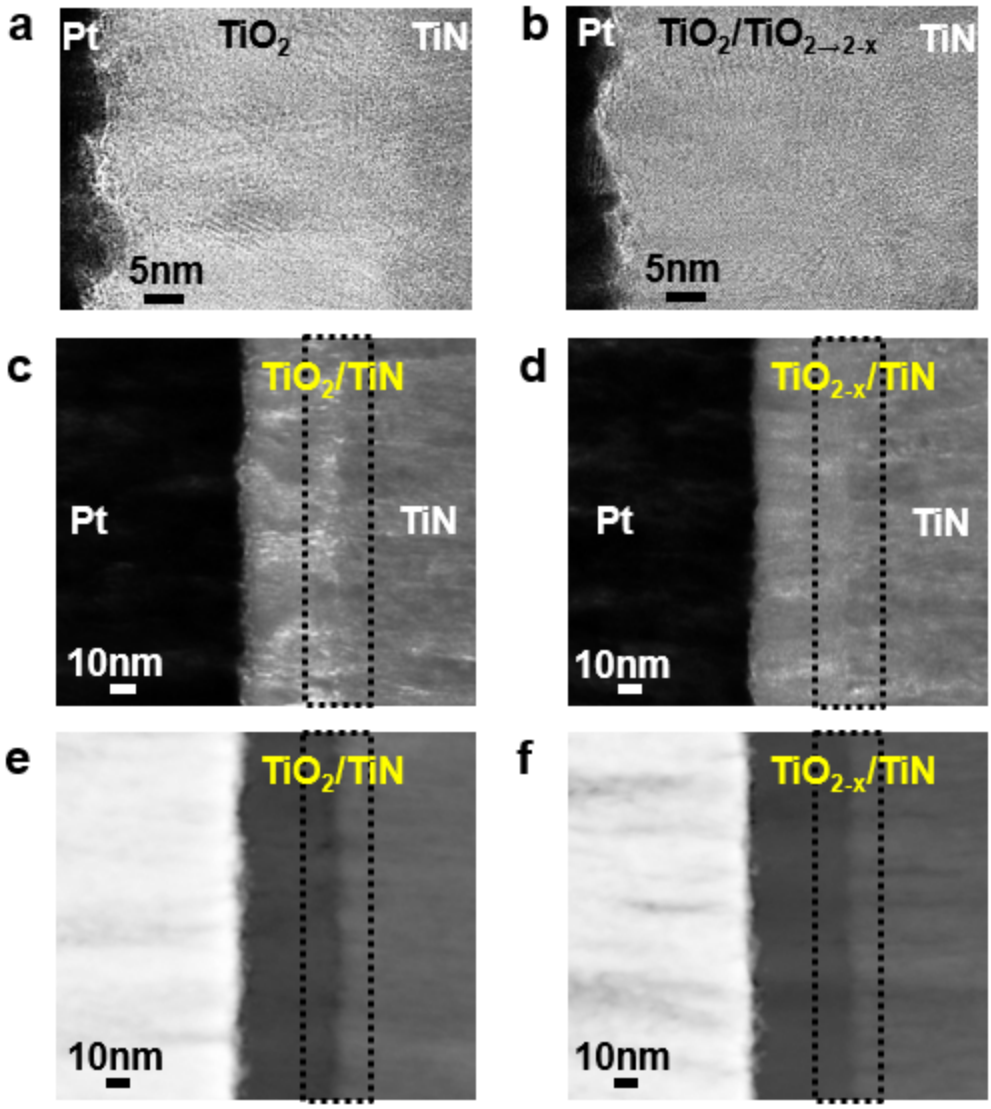
a
Pt
TiO2
TiN
5nm
b
Pt
TiO2/TiO2−2-x
TiN
5nm
c
TiO2/TiN
Pt
TiN
10nm
d
TiO2-x/TiN
Pt
TiN
10nm
e
TiO2/TiN
10nm
f
TiO2-x/TiN
10nm

Figure S3.

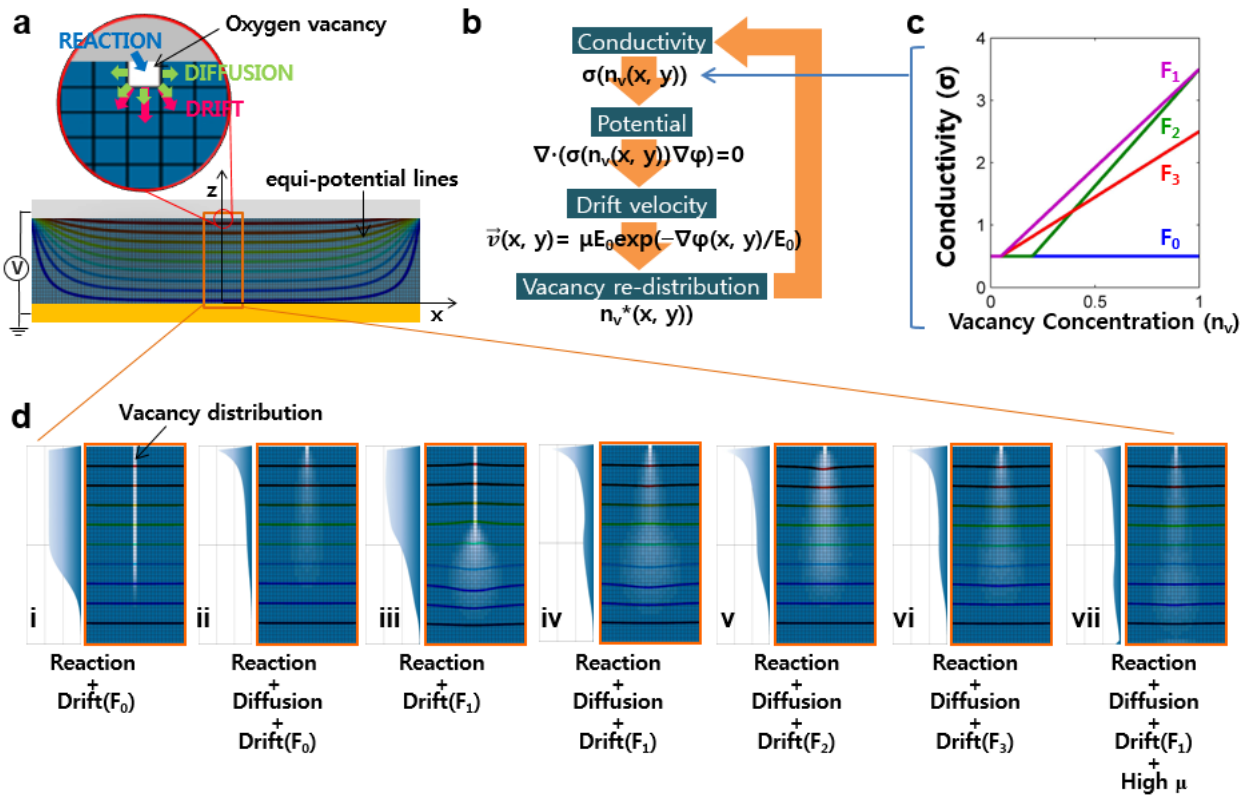
a
REACTION
Oxygen vacancy
DIFFUSION
DRIFT
z
equi-potential lines
V
x
b
Conductivity
σ(n_v(x, y))
Potential
∇·(σ(n_v(x, y))∇φ)=0
Drift velocity
v(x, y)= μE_0exp(−∇φ(x, y)/E_0)
Vacancy re-distribution
n_v*(x, y))
c
Conductivity (σ)
Vacancy Concentration (n_v)
F_1
F_2
F_3
F_0
d
Vacancy distribution
i
ii
iii
iv
v
vi
vii
Reaction + Drift(F_0)
Reaction + Diffusion + Drift(F_0)
Reaction + Drift(F_1)
Reaction + Diffusion + Drift(F_1)
Reaction + Diffusion + Drift(F_2)
Reaction + Diffusion + Drift(F_3)
Reaction + Diffusion + Drift(F_1) + High μ

Figure S4.

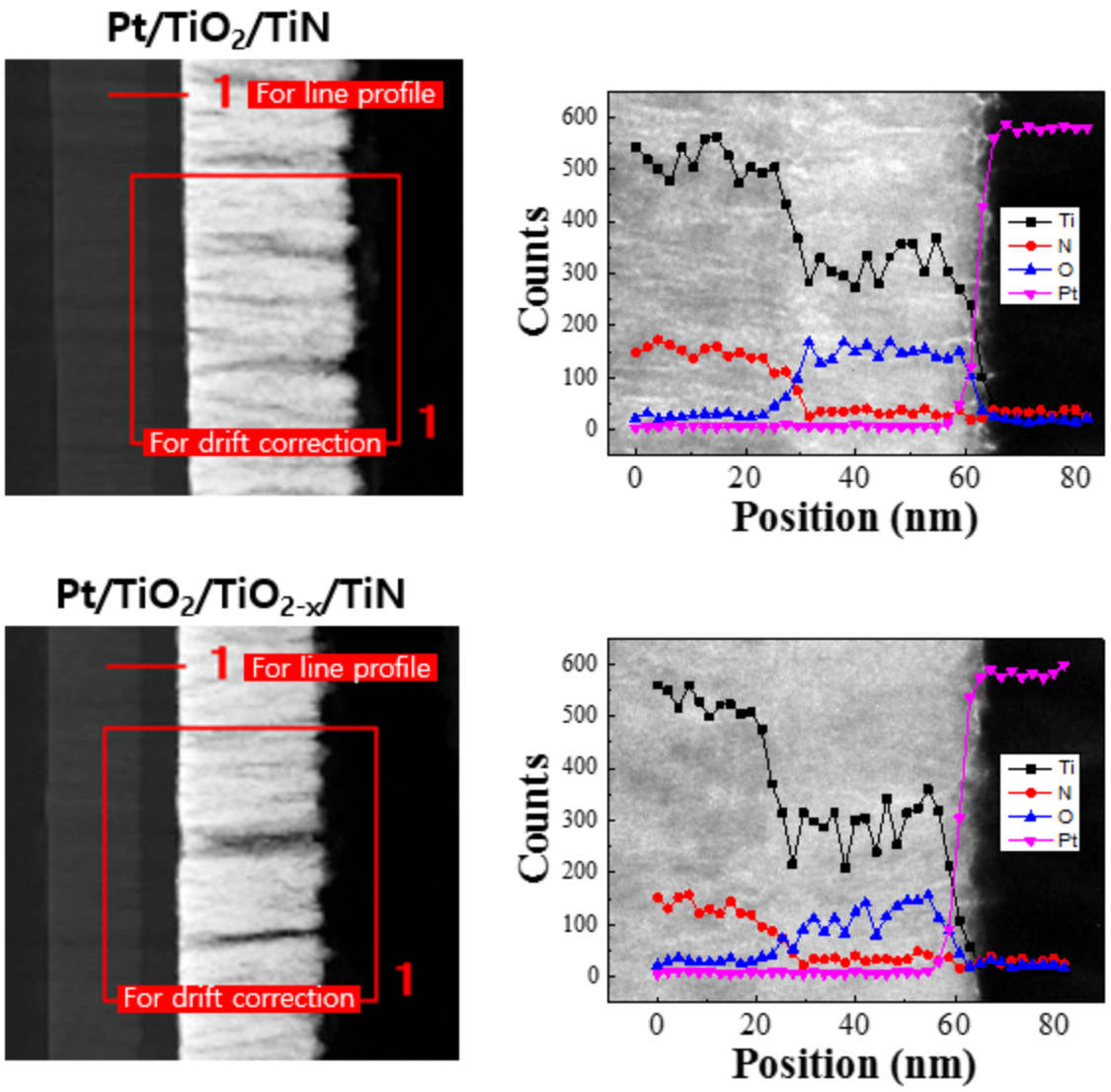
Pt/TiO2/TiN
1
For line profile
For drift correction
1
Counts
Position (nm)
Ti
N
O
Pt
Pt/TiO2/TiO2-x/TiN
1
For line profile
For drift correction
1
Counts
Position (nm)
Ti
N
O
Pt

Figure S5.

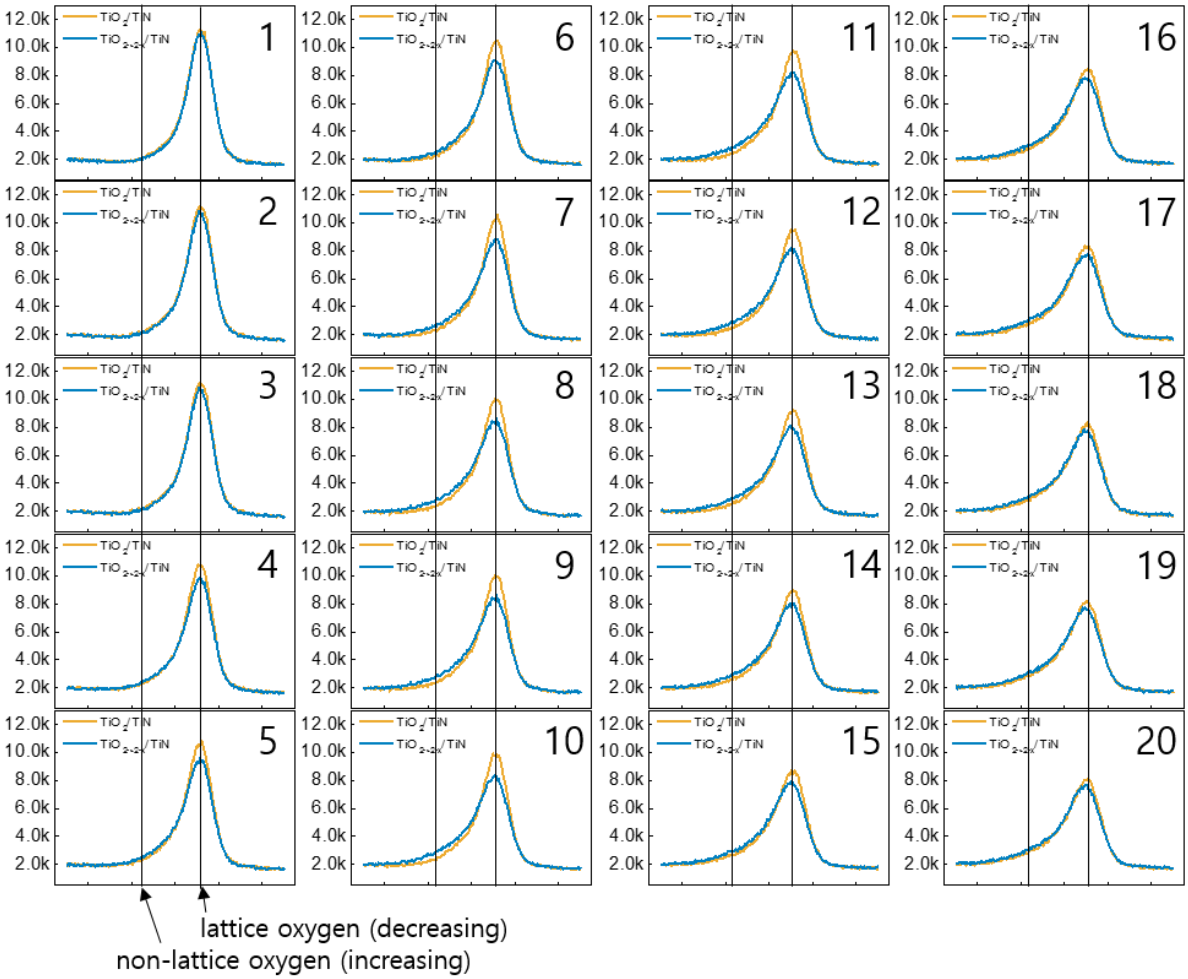
12.0k
10.0k
8.0k
6.0k
4.0k
2.0k
TiO2/TiN
TiO2-2x/TiN
1
2
3
4
5
6
7
8
9
10
11
12
13
14
15
16
17
18
19
20
lattice oxygen (decreasing)
non-lattice oxygen (increasing)